# On the dynamic nature of a quiescent prominence observed by IRIS and MSDP spectrographs

Guiping Ruan[1,2,3], Brigitte Schmieder[2], Pierre Mein[2], Nicole Mein[2], Nicolas Labrosse[4], Stanislav Gunár[5,2], Yao Chen[1]

1 Shandong Provincial Key Laboratory of Optical Astronomy and Solar-Terrestrial Environment, and Institute of Space Sciences, Shandong University, Weihai 264209, China; rgp@sdu.edu.cn

2 LESIA, Observatoire de Paris, PSL Research University, CNRS Sorbonne Université, Univ. Paris 06, Univ. Paris Diderot, Sorbonne Paris Cité, 5 place Jules Janssen, F-92195 Meudon, France

3 Key Laboratory of Solar Activity, National Astronomical Observatories, Chinese Academy of Sciences, Beijing 100012, China

4 SUPA School of Physics and Astronomy, University of Glasgow, Glasgow, G12 8QQ, UK

5 Astronomical Institute, The Czech Academy of Sciences, Czech Republic, 25165 Ondřejov, Czech Republic

Received _____; accepted _____

## ABSTRACT

Quiescent solar prominences are generally considered to have a stable large-scale structure. However, they consist of multiple small-scale structures that are often significantly dynamic. To understand the nature of prominence plasma dynamics we use the high spatial, temporal and spectral resolution observations obtained by IRIS during a coordinated campaign with the MSDP spectrograph at the Meudon Solar Tower. Detailed analysis of the IRIS observations of Mg II lines, including the analysis of Dopplershift and line width obtained with two different methods (quantile method, and gaussian-fit method) are discussed in the frame of the dynamic nature of the structures. Large-scale coherent blue and redshift features are observed in Mg II lines and H$\alpha$ exhibiting a slow evolution during 1:40 hour of observations. We explain the presence of several significantly asymmetric peaks in the observed Mg II line profiles by the presence of several prominence fine structures moving with different velocities located along the line of sight. In such a case, the decrease of the intensity of individual components of the observed spectra with the distance from the central wavelength can be explained by the Doppler dimming effect. We show that C II line profiles may be used to confirm the existence of multi-components along the line-of-sight.


*Subject headings:* Sun: spectroscopy —Sun: filaments, prominences

## 1. Introduction

Prominences have been observed for more than a century but they still hide many mysteries, particularly in their dynamic nature (Tandberg-Hanssen 1995). Several reviews describe the physical parameters of the prominence cool plasma embeded in the magnetic field (Labrosse et al. 2010; Mackay et al. 2010; Tandberg-Hanssen 2011; Schmieder et al. 2014a). Nevertheless, many questions remain with no answers. Thanks to the high spatial resolution and the high cadence of the recent space observations obtained with the *Solar Dynamics Observatory* spacecraft and its instrument the Atmospheric Imaging Assembly (AIA; Lemen et al. 2012) and the Solar Optical Telescope (SOT; Kosugi et al. 2007) on board Hinode, prominence fine structures are resolved. However, the remaining key problem is the understanding of their dynamics in a coherent view, because, it is difficult to relate the global structure of prominences to their fine structures. With the Swedish Solar Telescope (SST; Scharmer et al. 2003), the New Vacuum Solar Telescope (NVST; Liu et al. 2014) and New Solar Telescope (NST; Goode & Cao 2012) individual prominence/filament fine structures have been observed and their widths have been estimated to be lower than 0.3 arcsec (Lin et al. 2005, 2007; Yang et al. 2014; Yan et al. 2015; Shen et al. 2015). The dynamic nature of fine structures is so far difficult to explain with static modelings of magnetic field dips sustaining the prominence plasma (Aulanier & Démoulin 1998; Heinzel & Anzer 1999; Heinzel et al. 2001; Gunár et al. 2014). The interpretation of the apparent motions that we see in prominences: rising bubbles, plumes, horns, rotating tornadoes etc is still open for discussion (Berger et al. 2008; Heinzel et al. 2008; de Toma et al. 2008; Berger et al. 2010; Dudík et al. 2012; Li et al. 2012; Schmit & Gibson 2013; Su et al. 2014; Levens et al. 2015; Wedemeyer et al. 2013; Wang et al. 2016; Yang et al. 2018). After the past ten years it starts to be clear that prominences have a 3D complex structure where each pixel represents an integration of emission of all the fine structures along any line of sight crossing the volume of the prominence. It has been demonstrated that hedgerow prominence fine

structures are not hanging in the plane of the sky by chance but are the result of piles of dipped field lines aligned more or less quasi-vertically when seen in observed projection to the sky plane (Dudík et al. 2008, 2012). Spectropolarimetry of prominences showed that nearly all the prominences and also the prominence tornadoes have a preponderance to be supported by horizontal magnetic field (Lopez-Ariste 2014; Schmieder et al. 2013; Levens et al. 2016a,b). The *Interface Region Imaging Spectrograph* (IRIS) (De Pontieu et al. 2014) with its simultaneous imaging and spectral resolution capabilities is a very powerful tool for the investigation of the dynamics of the solar chromosphere and prominences. IRIS observations allow to infer the direction of the magnetic field from measured velocity vectors. If we assume that the cool material moves along the magnetic field lines in prominences, the velocity vectors then mimic the magnetic field configuration. For one helical prominence observed with Hinode/SOT and IRIS it was possible to follow small knots along magnetic loops in the plane of the sky and derive the transverse velocity field, which combined with the Dopplershifts allows us to derive the velocity vectors (Schmieder et al. 2017b). The Mg II line spectra and slit jaw images were used for this study. It was demonstrated that the knots were not following helical trajectories but moved along very shallow horizontal field lines pointing into the plane of the disk.

Spectroscopy allows to get good diagnostics of the physical parameters of prominences. Dynamics of prominences have been studied with ground-based spectrographs observing in chromospheric lines (H$\alpha$ and 10830 Å) and with space missions such as SMM/UVSP, SOHO/SUMER but with a relative poor cadence. Bulk motions in prominences have been determined with these instruments. It was clear that large velocities up to 20 km/s occurred along horizontal field lines in the main part of filaments (Schmieder 1990). Counter-streaming flows are also often visible along prominence spines (Zirker et al. 1998; Schmieder et al. 2004; Chen et al. 2014). In the barbs intermittent vertical flows (up or down) are frequently observed (Schmieder et al. 1991; Chae et al. 2008; Luna et al. 2018).

These inflows are nevertheless not sufficient to fill a filament with chromospheric material. For the formation of filaments, the evaporation-condensation models are still the most plausible (Karpen et al. 2005; Luna et al. 2012; Xia et al. 2014). With IRIS it is possible to study the dynamics of individual fine structures in eruptive prominences (Liu et al. 2015), in tornadoes (Levens et al. 2016a,b) and in quiescent prominences (Schmieder et al. 2014b). To interpret the behaviour of the Mg II chromospheric lines a NLTE (i.e. departures from LTE) radiative transfer approach is necessary (Heinzel et al. 2014, 2015; Rodger & Labrosse 2017).

In this paper we concentrate on the dynamics of a quiescent prominence observed during a coordinated campaign on March 30, 2017 using IRIS with Mg II, C II and Si IV lines and the Multichannel Subtractive Double Pass spectrograph (MSDP) operating at the Meudon solar tower with the H$\alpha$ line. In Section 2 we present the observed data, and in Section 3 the different methods to analyse the Mg II lines to determine Dopplershifts and line widths. Dopplershifts in H$\alpha$ and in Mg II are compared using histograms. In Section 4 we analyse individual Mg II profiles. We show that it is still unclear if complex profiles can be interpreted as composite profiles due to the presence of multiple prominence fine structures integrated along the line of sight or as single reversed profiles due to optical thickness of the lines. C II profiles suggest that such complex profiles could be indeed interpreted as composite profiles of multiple fine-structures having supersonic velocities.

## 2. Observations of the prominence

In this paper, we present a study of the dynamics of a quiescent prominence located on the West limb (N45). On the disk the prominence is observed as a long filament oriented mainly East West with dark bushes which correspond to its anchorages in the photosphere on March 25 2017 (Figure 1a). The prominence (30 to 50 arcsec height) was observed by

multiple instruments on the ground and in space on March 30, 2017 (Figure 1 b, c, d, e). Instruments used for these observations include the IRIS, SDO/AIA and the MSDP spectrograph at the Meudon Solar Tower. IRIS provided line profiles in Mg II h (2803.5 Å) and k (2796.4 Å), C II doublet (1334.5 Å, 1335.7 Å) lines and Si IV (1402.8 Å and 1393.8 Å) lines along 32 slit positions, MSDP provided H$\alpha$ (6563 Å) line profiles in a two-dimensional field of view. The prominence appears as a dark absorption area in 171 Å and a bright structure with two horn-like structures at the top in 304 Å as it is observed in several data (Schmit & Gibson 2013).

### 2.1. MSDP

The Meudon MSDP observations of prominence in H$\alpha$ consist of series of five spectral images with 10″ overlaps in each time sequence, which allow to obtain a field of view of 450″x230″. Sequences of observations are done during 15 min with a 30s cadence. The obtained data have been processed with the MSDP software (Mein et al. 2001). On March 30 2017, three sequences of observations were done between 07:28:54 UT and 08:55:28 UT (Table 1). We focus our study on the sequences covering the interval of the IRIS observations (Figure 2). The exposure time is 100 ms for the first sequence and 150 ms for the two next sequences. In each MSDP pixel an H$\alpha$ line profile is obtained over a wavelength range of +/-0.7 Å. Background subtractions are used to reduce scattering effects on line profiles.

The H$\alpha$ prominence consists of two triangular areas with a nearly empty space between them. In the IRIS these areas are located in the Mg II slit jaw image, however more fine structures are observable by IRIS at higher altitudes (Figure 2).

### 2.2. IRIS

IRIS performed a 32-step coarse raster observation from 07:06 UT to 08:46 UT on March 30, 2017 (Figure 3). The pointing of the telescope is 722″, 684″ (Table 1). The spatial pixel size is 0.3327″. Slit-jaw images (SJI) in the broadband filters (1330 Å, 1400 Å and 2796 Å) were taken at a cadence of 126 s. The 1400 Å slit jaw is an integration of the FUV emission within a range of about 40 Å. The FOV was 167″×175″ for the SJIs.

Calibrated level 2 data are used in this study. Dark current subtraction, flat field correction, and geometrical correction have been taken into account in the level 2 data (De Pontieu et al. 2014).

We used the spectra in Mg II (2796.4 Å, 2803.5 Å), Si IV (1393.8 Å, 1402.8 Å) and C II (1334.5 Å, 1335.7 Å) lines and the SJI 1400 Å and 2796 Å data for this study. The SJI 1400 Å filter emission includes the total emission of the Si IV 1402 Å and 1393 Å lines formed in the prominence corona transition region (PCTR) and the SJI 2796 Å emission mainly from the Mg II k line. The Mg II h and k lines and C II lines are formed at chromospheric temperatures e.g. between 8000 K and 15000 K (De Pontieu et al. 2014; Alissandrakis et al. 2018). The coalignment between the different optical channels of IRIS was achieved by checking the position of the horizontal fiducial line.

Table 1:: List of observations of IRIS and MSDP on March 30, 2017.

| Instrument | Time Sequence UT | Raster Characteristics | | Lines | | Temperature | SJI Characteristics |
|---|---|---|---|---|---|---|---|
| *IRIS* | 07:06-08:46 | Pointing: | 722″,684″ | | | | |
| | (07:06-07:22 | Field of View (FOV): | 62″x175″ | | | | FOV: 167″x175″ |
| | 07:23-07:39 | Steps: | 32x2″ | Mg II k: | 2796.4 Å | $10^4$K | 2796 Å |
| | 07:39-07:56 | Step Cadence: | 31.4 s | Mg II h : | 2803.5 Å | $10^4$K | |
| | 07:56-08:12 | Raster Cadence: | 16.75min | C II: | 1402 Å,1393 Å | $10^4$K | 1400 Å |
| | 08:13-08:29 | Spatial Resolution: | 0.″3327 | Si IV: | 1334 Å,1335 Å | $10^5$K | 1330 Å |
| | 08:30-08:46) | | | | | | Time Resolution: 126s |
| MSDP | 07:28-08:55 | FOV: | 450″x230″ | H$\alpha$: | 6563 Å | 8000K | |
| | (07:28-07:43 | Time Resolution: | 30 s | | | | |
| | 07:52-08:22 | Pixel Size: | 0.″5 | | | | |
| | 08:25-08:55) | | | | | | |

## 3. Dopplershifts in the prominence

### 3.1. Dynamics of the prominence

The IRIS SJI movie shows a high activity of the structures (see the movie attached to Figure 3 top left). The raster cadence of the spectral observation in both the near ultraviolet (NUV 2784-2834 Å) and the far ultraviolet (FUV 1332-1357 Å and 1382-1406 Å) was 31.4 s. The exposure time is 30 s. This long exposure time leads to a low raster cadence of 1005 s. Therefore only six raster images (62″x175″) can be reconstructed from the spectra during one hour and 40 minutes observation with a raster step of 2 arcsec. The bottom panels of Figure 3 show three of the six raster images reconstructed by using the central intensity value in the Mg II k line profile. Multiple structures are observed inside the prominence with a kind of an empty bubble between two triangles. The North triangle has a double structure at the top like two semi circular loops similar to the two horns visible in

304 Å (Figure 1 e). There is a great difference of the fine structures between two successive images obtained in 15 minutes each. The long exposure time allows to get a relatively good signal for C II and Si IV lines.

### 3.2. Zero velocity reference wavelength in Mg II and C II lines

Mg II and C II profiles have been calibrated by the code of Hui Tian using the IRIS reference spectra of 2016. Before computing the Dopplershifts, the zero velocity reference must be defined. To do so we choose to use the line profiles observed on the solar disk that are present in the raster spectra. In this way we obtain an average profile of the quiet sun near the limb (Figure 4). The zero velocity reference wavelength is defined by the minimum of the average intensity in the core of the Mg II lines. For Mg II k we found the zero velocity reference wavelength at 2796.3578 Å and for Mg II h it is at 2803.5375 Å. Another way to define the zero reference wavelength is to fit the averaged profile over the disk by a gaussian function. We define the zero reference wavelength at the maximum intensity of the gaussian function. The difference between the two derived values is small (- 0.017 Å). This corresponds to a velocity precision of 1.78 km/s. For the C II line, the zero velocity reference is chosen by the maximum of the fit with a gaussian function because the average of the C II line profiles is complex. The two lines of C II are centered at 1334.5360 Å, and 1335.7212 Å respectively.

### 3.3. Two methods for computing Mg II Dopplershifts

Figure 5 shows a zoom of the Mg II line profiles for two slits. Along the slit 18 (top), the Mg II h and k profiles are all broad with a self-absorption core in the central section of the slit. In contrast along the slit 21 (bottom) there are many thin profiles lacking a central

reversal between pixels 150 and 220. Taking into account the general shape of the profiles, it seems reasonable to compute the Dopplershifts by fitting the profiles with a gaussian function. This assumption is confirmed by the comparison of the results obtained with another method which does not depend on the shape of the profiles. The second method is the quantile method. It consists in calculating the cumulative distribution function (CDF) of the normalized intensity profile as a function of wavelength. The line centroid ($Q2$) is then given by the wavelength position of the 50% level of the CDF. The line width is given by the difference in wavelength between the 88% level ($Q3$) and the 12% level($Q1$) of the CDF. With this convention, the line width of a Gaussian profile obtained by this method is equal to the standard Full Width at Half-Maximum. Finally, the profile asymmetry is defined as

$$S = \frac{(Q3 - Q2) - (Q2 - Q1)}{Q3 - Q1} \ .$$

This method was successfully used to analyse flare spectra by Kerr et al. (2015).

Figures 6 and 7 present the LOS velocity and the width of Mg II k line for raster 2 between 07:23:14 and 07:39:27 UT. The Dopplershift maps have comparable patterns with a mixture of blue and redshifts close to the limb and a blue area at the top of the prominence. The width pattern is also comparable. Figure 8 presents the values of the integrated intensity, LOS velocity and profile width along the slit 21 (see Figure 3 (top-left)) obtained by both methods. In the main part of the prominence between pixels 220 and 300, the Dopplershifts obtained with the two methods are nearly the same. The widths of the profiles for 50% of the integrated intensity are relatively large (0.4 Å to 0.6 Å). Close to the limb (pixels 150 to 220) the profiles are very narrow as Figure 5 shows. Their widths are around 0.2 Å as obtained with the gaussian method and reach 0.6 Å in some pixels as obtained with the quantile method. This region corresponds to low values of intensity and to the empty bubble visible in Figure 2 at (735″, 660″). The differences in the width values between the two methods are due to the presence of a secondary peak along the

main profile (pixels 200-215) which is taken into account by the quantile method and not by the gaussian method. The velocities are also different. We discuss these profiles in the next section. In the fine structure blobs at higher altitudes (pixels 340-350), the values are similar.

### 3.4. Time evolution of Dopplershift pattern in Mg II line

Figure 9 shows the evolution of the Dopplershift pattern obtained from the IRIS spectra during one hour and forty minutes. Each plotted map is obtained during 15 minutes scanning time. The blue area indicated by the arrow A is changing progressively to red. The red area indicated by the arrow B in the raster 2 becomes blue in the raster 6. Close to the limb a blue area indicated by the arrow C increases in size and reaches the blue area of the prominence top in the last map. The evolution appears to be slow, as it takes more than 60 minutes to recover the initial Dopplershift pattern. This suggests the existence of long period oscillations.

In the first map (07:06:26-07:22:42) the left semi circular structure (horn-like) at the top of the prominence exhibits blue and red shift along its axis suggesting some possible rotation like in tornado (Su et al. 2014; Levens et al. 2015). However the blue horn-like is well visible in the first map, but it becomes red in the fourth and fifth map and back to blue in the sixth map.

### 3.5. H$\alpha$ Imaging Spectroscopy

Dopplershifts are computed for the three observation sequences of the MSDP spectrograph lasting in total 87 minutes (see Table 1). The first sequence lasts 15 minutes. After a gap of 9 minutes the second sequence lasts 30 minutes. After another gap of 3

minutes the last sequence lasts also 30 minutes. The zero velocity reference wavelength is chosen by the average value of the Doppler velocity in the prominence over all 150 obtained Dopplergrams. Around 6000 pixels cover the prominence in a single Dopplergram.

Figure 10 shows an example of five Dopplergrams from the 150 Dopplergrams obtained during the three sequences of observations by the MSDP. These five Dopplergrams correspond approximatively to the middle time of the five of the six IRIS rasters. The first raster of IRIS has been obtained before the beginning of the MSDP observations. In the H$\alpha$ line we have no information about the high structures visible with IRIS. However, we see a similar time evolution of the large Dopplershift pattern in the main part of the prominence detected by both instruments with the same order of magnitude of the LOS velocity. We note that the H$\alpha$ Dopplershift pattern evolves like the pattern in Mg II (Figure 10). The blueshift area at the top of the North triangle in region A at 07:31 UT becomes red at 08:21 UT and starts to be blueshifted at 08:38 UT. In the South triangle (region B) a large redshift area is observed at 08:07 UT, the area is decreasing in size and is replaced by blueshift area at 08:38 UT. Such Dopplershift pattern has been observed in other prominences (Schmieder et al. 2010, 2017a). Long sequences of Dopplershift observations of a prominence-tornado showed such an evolution. The authors have suggested that long quasi-periodic oscillations (40 to 60 minutes) could exist. Here the periodicity could be estimated to 60 minutes however the sequence lasts only 87 minutes, so it is a relatively short time to derive a definitive conclusion on the existence of 60 minutes oscillations.

### 3.6. Comparison of H$\alpha$ and Mg II Dopplershifts

IRIS and MSDP spectrographs provide a large amount of spectral observations of the studied prominence. This allows us to statistically compare the LOS velocities derived from both data sets. In Figure 12 we show two sets of histograms corresponding to the IRIS

rasters 2 and 4. In each panel of Figure 12 we plot normalized histograms of LOS velocities derived from MSDP (blue lines) and from IRIS. For IRIS we plot with red lines results from the area corresponding to the MSDP prominence (see Figure 9) and with green lines results from the entire prominence visible in the IRIS rasters.

The comparison between the histograms displaying the entire IRIS prominence (green) and the IRIS data corresponding to the MSDP prominence (red) shows an excess of rather high velocities (± 20-30 km/s) present only in the entire IRIS prominence histograms. This suggests that such velocities are measured in the part of the prominence not visible in H$\alpha$ and concentrated at the top of the prominence observed in Mg II. (see Figure 9). It is confirmed when we consider only pixels with velocities V>+9 km/s and V<-9 km/(Figure 11). We also see that large velocities are present at the edge of the prominence and the empty void or bubble.

From Figure 12 it is also clear that the LOS velocities obtained from the H$\alpha$ MSDP observations have, in general, lower values than the velocities derived from the Mg II IRIS observations. We note that the blue and red histograms are produced from the same area in the prominence and cover the same time interval. However, during this time interval MSDP provides several observations of the entire prominence while IRIS scans the prominence with the slit.

There are two complementary explanations for this difference. The first is the fact that the MSDP observations have lower spatial resolution than the IRIS observations. This means that any smaller-scale velocity features observed by IRIS are in the MSDP observations averaged over a larger area. Such an averaging will make the derived LOS velocities from the MSDP observations to be lower that those derived from the IRIS observations of the same structures. However, as is apparent from Figure 9, the LOS velocity features in the IRIS rasters are relatively large scale. This indicates that the

difference in the spatial resolution of the two instruments might not account for the entire difference in the derived LOS velocity values. The second effect that plays a role in the determination of the LOS velocities from observed Dopplershifts is the optical thickness in the used spectral line. The H$\alpha$ line observed by MSDP has in a typical prominence an optical thickness of the order of unity. The Mg II line has a typical optical thickness of the order of 100. Therefore, in the case where multiple prominence fine structures are aligned along the given LOS, any Dopplershifts of individual fine structures will be integrated along that LOS in the case of the H$\alpha$ line (see e.g. Gunár et al. 2012). On the other hand, in the case of the Mg II line the observed Dopplershifts will be dominated by the Dopplershift of the foremost thread. This effect will cause the LOS velocities derived from the H$\alpha$ observations to have, in general, lower values than those derived from the Mg II observations. This is valid in a case where multiple fine structures have different true LOS velocities with respect to each other. In the following section we show that such a situation may occur in the studied prominence.

## 4. Multiple prominence fine structures

In many places in the observed prominence the Mg II profiles show rather complex shapes. An example of such profiles is shown in Figure 13. In this figure we plot the Mg II k line profiles with respect to the LOS velocity (Dopplershift). This example shows several types of line profiles. Some profiles are rather narrow (188, 194) while others are very broad and complex, exhibiting multiple peaks (227, 238, 244). Moreover, several profiles show distinct lateral components (183, 198, 208, 212). These components are well separated in the velocity space and the intensity between them is very low. Such a wide and deep separation of the peaks can not be interpreted as a single profile with a reversal. However, such profiles can result from a situation where several prominence fine structures

with different LOS velocities are observed along the same LOS. These multi-component profiles typically have a more intense central component and weaker Dopplershifted lateral components. The intensity decrease of the lateral components can be explained by the Doppler dimming effect, as was demonstrated by Heinzel et al. (2015).

The fact that the multi-component Mg II k profiles are formed by multiple fine structures integrated along the LOS can be supported by analysis of the C II spectra observed by IRIS (see Figure 4). Both Mg II and C II lines are formed at similar temperature (log T=4 and log T=4.3, respectively). Therefore, individual components of both spectral line profiles that correspond to the same LOS velocity can be expected to be formed in the same fine structure along the LOS. In Figure 14 we show an example of several instances where the multi-component spectral profiles observed at the same position in the prominence exhibit the same Dopplershifts of their individual components. In this figure C II profiles are obtained by averaging over three adjacent pixels to increase the signal/noise ratio. We note that in both spectral lines the secondary components are weaker, which again indicates the influence of the Doppler dimming (see Heinzel et al. 2015 for more details). We also note that the LOS velocities of the secondary peaks can be as high as 45 km/s, which could be considered to be supersonic values.

When we take into account these examples it is possible to assume that the broad, complex profiles (pixels 227, 238, 244 in Figure 13) are also a superposition of profiles originating in different prominence fine structures located along the line of sight. However, while we are able to demonstrate this assumption on distinctly multi-component profiles (such as those shown in Figure 14), the complex profiles will require more detailed investigation. We will focus on this topic in our future work.

## 5. Conclusion

We analyzed the spectra of a quiescent prominence observed for one hour and a half on March 30 2017 during a multi-instrument campaign with IRIS and the MSDP operating on the Meudon solar tower. The prominence is intrinsically dynamic, even for a quiescent one. This may have been recognized only in a few prominences (Schmieder et al. 2014b; Yang et al. 2018). This study may be one of the few studies which uses spectroscopic data from different spectrographs (ground based and space instruments) to support the argument, and further suggests with spectral evidence the presence of multi-component structures along the LOS by the Doppler dimming effect (Heinzel et al. 2015).

In the first attempt the IRIS Mg II profiles were fitted with a single Gaussian function and with the quantile method. The two methods give similar widths and Dopplershifts in most of the prominence pixels when the width is relatively large (0.4 Å - 0.6 Å). For pixels with narrow widths there is a large discrepancy. We explain later the different results by discussing individual profiles and by the presence of multiple fine structures along the line of sight with different Dopplershifts.

The Doppler pattern of the prominence obtained in the Mg II k and h lines shows large areas of coherent velocities. A similar Doppler pattern is also obtained in the H$\alpha$ line with a relatively good spatial correspondence. The histograms of IRIS and MSDP inside the contours of the MSDP prominence with strong emission show that the Dopplershift values are between $\pm$ 6-10 km/s, slightly lower values in H$\alpha$ than in Mg II lines. If we assume that the transverse velocity is of the same order, it means that the plasma is moving in one hour by 20 000 km which could be a displacement of 27.6 arcsec. In fact the intensity shape of the global prominence does not change, so Dopplershifts in these areas may only concern quasi horizontal structures. In case of frozen plasma in magnetic field lines, the prominence that we observed is mainly supported by horizontal magnetic field parallel to the solar

surface and more or less perpendicularly to the plane of the sky. We know from previous studies that the optical thickness in H$\alpha$ is much lower than that of Mg II. The prominence plasma is optically thick in Mg II h and k lines, while it is (approximately) optically thin in H$\alpha$. Similar Dopplershifts in H$\alpha$ and Mg II lines indicate that in the prominence coherent motions are observed in volumes extended along the line of sight. Individual threads throughout the prominence exhibit motions with small relative amplitudes. On the other hand, large velocities observed by IRIS in Mg II resonance lines are not seen in H$\alpha$ MSDP data due to the weaker emission in that line and the lower spatial resolution of MSDP in comparison to IRIS.

The Doppler pattern versus time in Mg II lines as well as in H$\alpha$ evolves slowly during the 1 hour and half observation time with large cells changing from blue to red. This kind of evolution has been previously observed in a prominence-tornado (Schmieder et al. 2017a). The authors have suggested that such quasi periodicity could correspond to large scale and long period of oscillations (40 to 60 minutes). Our sequence is nevertheless slightly too short to completely confirm such an interpretation.

However looking carefully at the IRIS spectra, we found that the IRIS Mg II profiles are very different from each other, e.g. one single peak, two separate single peaks with a very low intensity value between the peaks and complex broad profiles with multiple peaks.

For example the structure with double semi-circular components at the top of the IRIS prominence has single peak Mg II profiles with measured Dopplershifts which can reach 20-30 km/s. This double structure mimics the horns that have been frequently detected in prominence cavities (Schmit & Gibson 2013; Chen et al. 2014). We have not analyzed in details the cavity of this prominence in the AIA images. But we do not see a clear curved emission structure in 171 Å images to prove the existence of typical horns. Along the highest and longer structure we distinguish blue and red shift symmetrically to its axis

suggesting a possible rotation. One could interpret this as some kind of tornado turning around its axis as it has been observed with Hinode/EIS (Su et al. 2014; Levens et al. 2015). However after half an hour the blue area becomes a red area and vice-versa. In fact it is difficult to understand the plasma motion inside this horn-like structure observed in the sky plane because it is a 3D structure. The IRIS movie of Mg II slit-jaws suggests instead more that this flow could correspond to a counter-streaming flow along large loops, changing direction with time (Zirker et al. 1998). We should be able to reconstruct the horns in 3D using the slit jaw images and the spectra of IRIS obtained simultaneously to understand the nature of this horn-like structure (Schmieder et al. 2017b).

Inside the main part of the prominence, broad profiles with double peaks are often observed. Since the spectral profiles are integrated over 30 s, the temporal evolution (heating, cooling) may also contribute to the complexity of the interpretation of spectral profiles. However we have demonstrated that two peak profiles in some cases correspond to two different structures with Dopplershifts which could reach 45 km/s. These supersonic flows belong to individual threads visible either at the top of the prominence or in front of the relatively empty void (bubble). We confirm these large Dopplershifts by using the C II lines which show equivalent Dopplershifts. Therefore the broad complex profiles could be interpreted by the existence of multiple fine structures along the line of sight and not only by large optical thickness as it is done frequently (Levens et al. 2016a).

With isobaric, isothermal models in a non LTE approach, the single profiles could correspond to narrow threads with thin plasma ($p < 0.01$ dyn/cm$^2$), while the complex profiles could also correspond to thicker plasma ($p = 0.2$ to $0.5$ dyn/cm$^2$) (Heinzel et al. 2014). However it has been demonstrated that the PCTR has an important contribution for the formation of the Mg II lines and it is not evident that such conclusion is valid for this prominence (Heinzel et al. 2015). A more detailed analysis using a multi-thread

model (Gunár et al. 2007, 2008; Labrosse & Rodger 2016) will be performed in the future combining H$\alpha$ and Mg II lines.

This analysis shows that the dynamic fine structures in prominences are not randomly distributed but organized in larger structures gathering them together as it was shown with coherent velocity structures. The observations commonly integrated different parts of the prominences and it is difficult to have a 3D view of the different spatial scales of the velocity and intensity structures. Higher spatial resolution and spectroscopic data should be provided by the new telescopes (NVST in Kunming, NST in Big Bear, DKIST in Hawaii and EST in Canary Islands).

G.P. Ruan and Y. Chen acknowledge the support by the NNSFC grant U1831107, 41774180, 41331068, 11790303(11790300), the CSC scholarship, Provincial Natural Science Foundation of Shandong (Grant No. ZR2018MA031) to SDUWH and and the Key Laboratory of Solar Activity of the Chinese Academy of Sciences (CAS) under the grant number KLSA201602. S.G. acknowledges the support from grant No. 16-17586S and 16-18495S of the Czech Science Foundation (GAČR). N. Labrosse acknowledges support from STFC grant ST/P000533/1. S.G. thanks for the support from project RVO:67985815 of the Astronomical Institute of the Czech Academy of Sciences and the financial support from the Observatoire de Paris through its ″Postes Temporairement Vacants″ programme during his visit at LESIA. G.P. Ruan thanks the LESIA at the Observatoire de Paris to welcome her having one year Chinese fellowship. We are grateful to Barczynski Krzysztof, Bing Wang, Zihao Yang and Zhenyong Hou for their discussions. We thank for Dr. P. Heinzel for his fruitful discussion and Dr Hui Tian for his IRIS code for calibration. We thank SDO/HMI, SDO/AIA and IRIS science teams for the free access to the data. This work was inspired from meetings of the ISSI International Team managed by N. Labrosse on ″Solving the Prominence Paradox″. We are grateful to observers at the solar tower

(Regis Lecocguen and Daniel Crussaire).

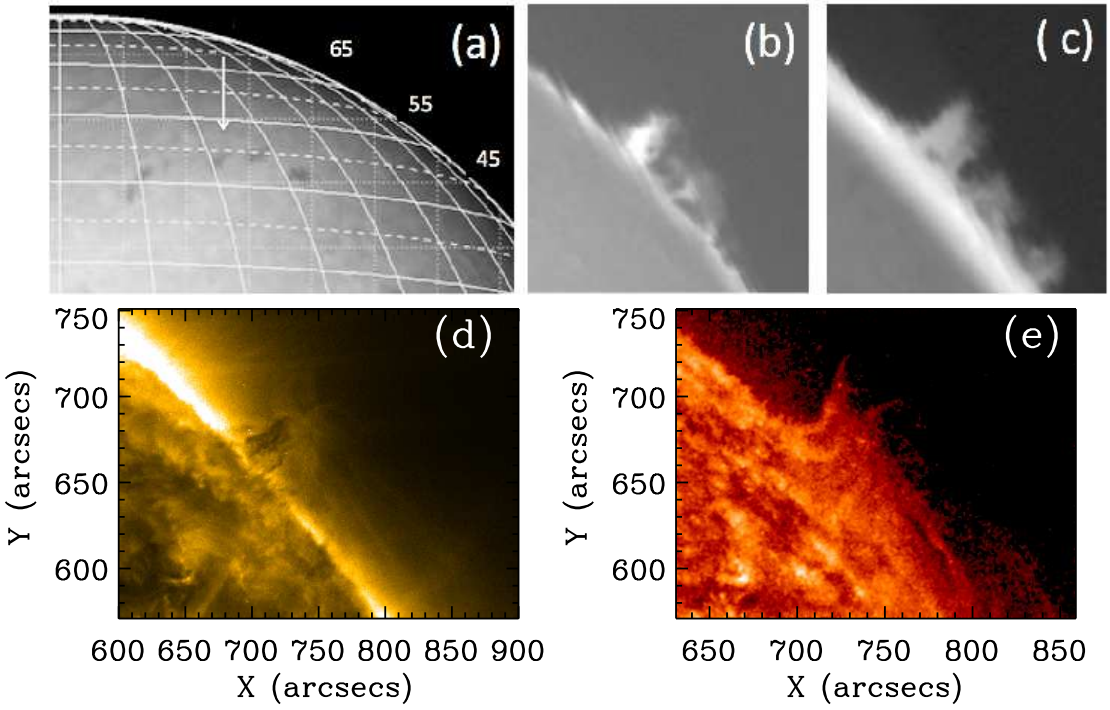


Fig. 1.— (a) Filament observed by the Meudon spectroheliograph on March 25, 2017; the arrow indicates the part of the filament, which appears at the limb on March 30 2017. Prominence observed by the Meudon spectroheliograph at 06:48:17 UT (b) and 15:11:47 UT ( c) on March 30, 2017 (Meudon solar survey data center BASS2000). Bottom panels show SDO/AIA 171 Å (d) and 304 Å (e) images of the prominence on March 30 2017 at 07:28 UT.

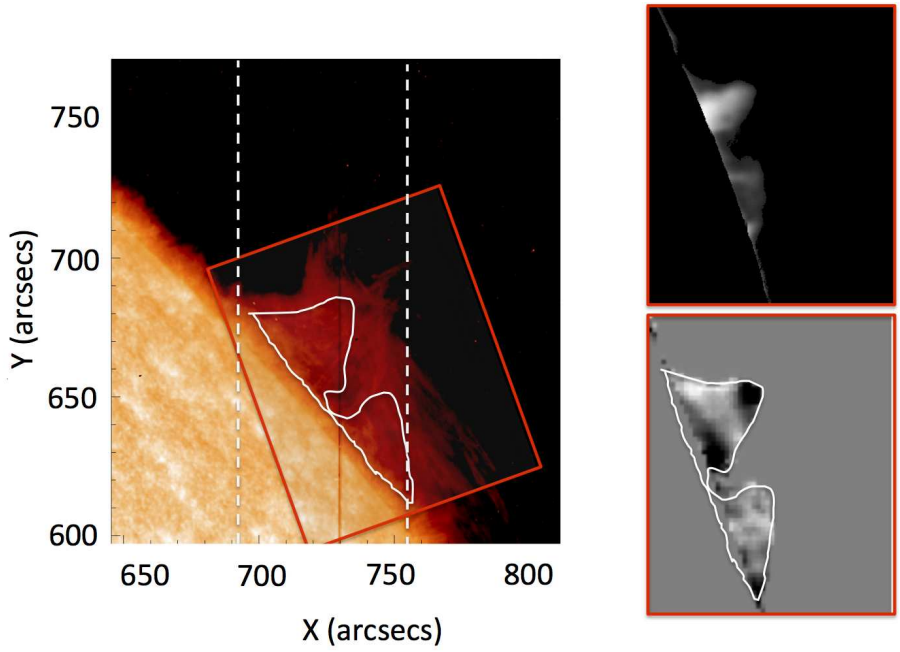


Fig. 2.— (left panel) IRIS SJIs in 2796 Å on March 30, 2017 overlaid with white contours of the MSDP prominence and the red box which is the field of view from the right panels. (right panels) MSDP prominence intensity (top) and Doppler shift observed in H$\alpha$ (bottom) on March 30, 2017 at 07:28 UT. Black and white indicate blueshift/redshift limited to $\pm$7 km s$^{-1}$. The two dashed vertical lines in the IRIS SJI image show the field of view of the IRIS rasters (see Figure 3). The red vertical line indicates the slit 20. An animation of the slit-jaw images (SJI) in the broadband 2796 Å filter is available in the online Journal. The animation covers from 07:08 to 08:46 UT and is not annotated.

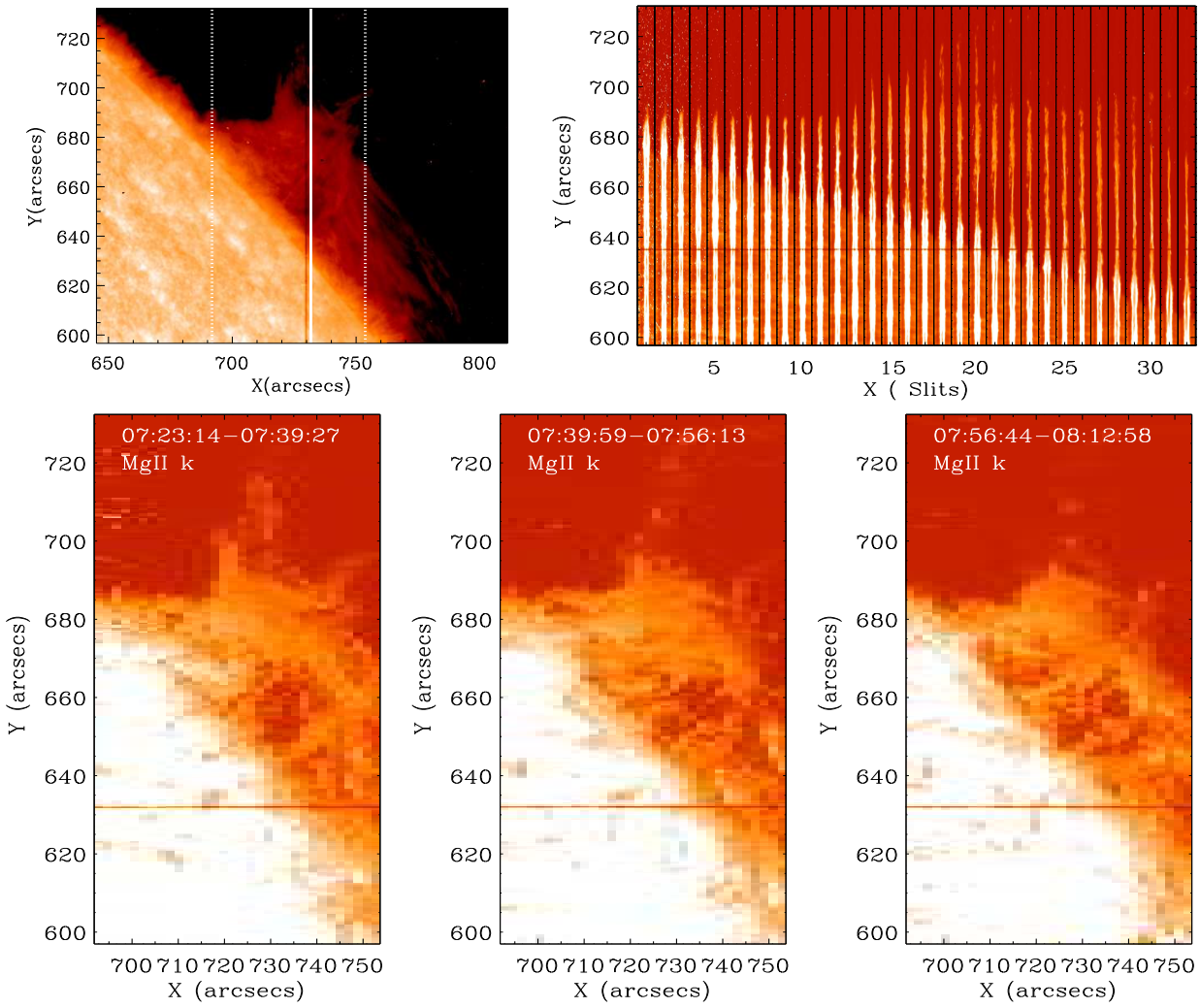


Fig. 3.— (top left) IRIS SJI image of the prominence in Mg II k 2796 Å filter. Dashed-white vertical lines highlight the extend of the rasters. The middle, red vertical line indicates the slit 20 and the nearby (solid-white) line indicates the slit 21. (top right) 32 spectra in 2796 Å Mg II line obtained between 07:23:14 UT and 07:39:27 UT are plotted side-by-side, showing the bright solar disk and the faint prominence emission between 596.96″ and 732.37″. The dark horizontal line at pixel 120 is a fiducial line used for the alignment of the different lines in the IRIS spectra. (bottom panels) Intensity maps reconstructed from central intensity of the Mg II k spectra. We note a void (bubble) in the prominence at (735″, 660″). An animation of the slit-jaw images and 32 side-by-side spectra is available in the online Journal. The animation covers from 07:08 to 08:46 UT and is chunked into 6 approximately 15 minute averages.

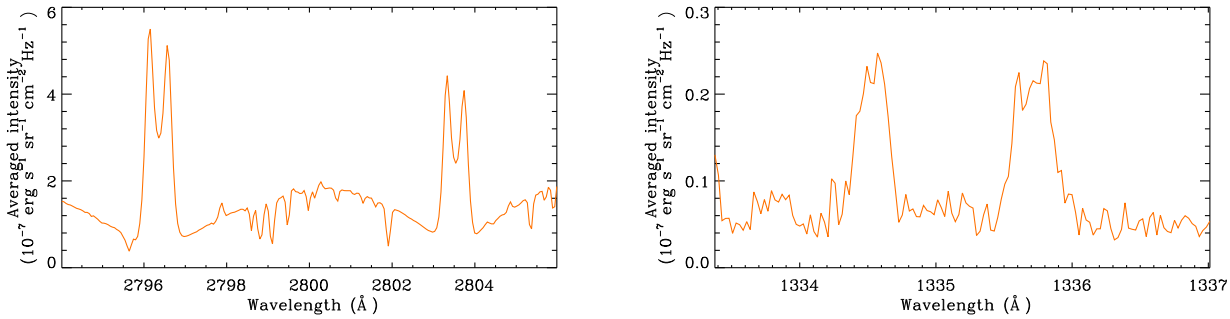


Fig. 4.— Averaged spectral profile of the Mg II lines (left panel), and averaged spectral profile of the C II lines (right panel) observed by IRIS on the quiet sun close to the limb on March 30, 2017. Profiles are spatially averaged over parts of the solar disk that are present in the entire raster 2. Mg II k is centered on 2796.3578 Å, Mg II h is centered on 2803.5375 Å. These values are used as the zero velocity reference wavelengths.

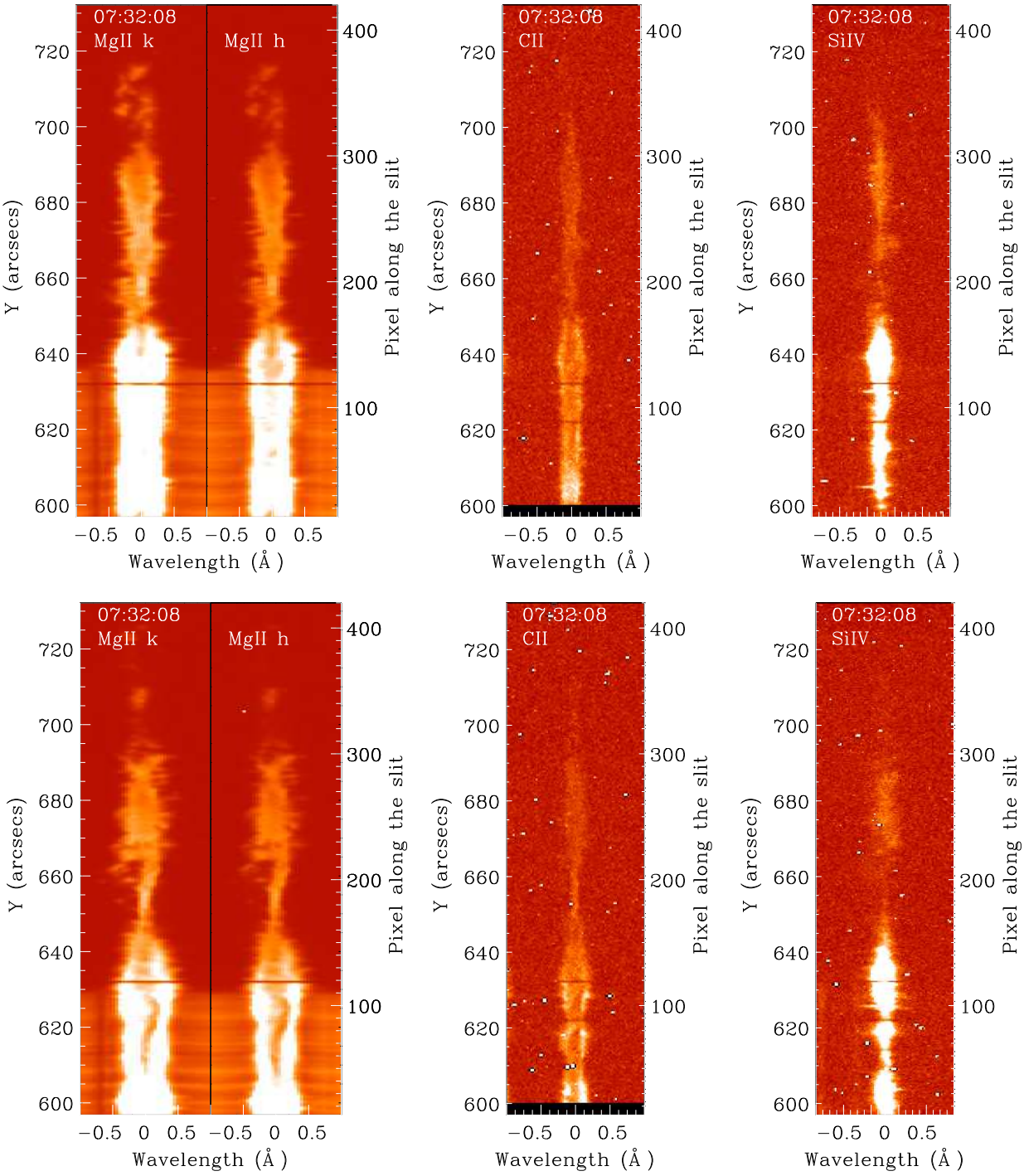


Fig. 5.— Examples of IRIS spectra of Mg II k and h lines, C II and Si IV lines for slit 18 (top) and slit 21 (bottom). The Mg II k line is centered on 2796.3578 Å, Mg II h on 2803.5375 Å, C II doublet at 1334.5360 and 1335.7212 Å and Si IV line at 1393.7694 Å. The y-range in each panel shows the solar-y coordinate on the left and pixel coordinate on the right. The solar disk is between pixel 0 and pixel 120, the spicule region between pixel 120 and pixel 150, the prominence between pixel 150 and pixel 380.

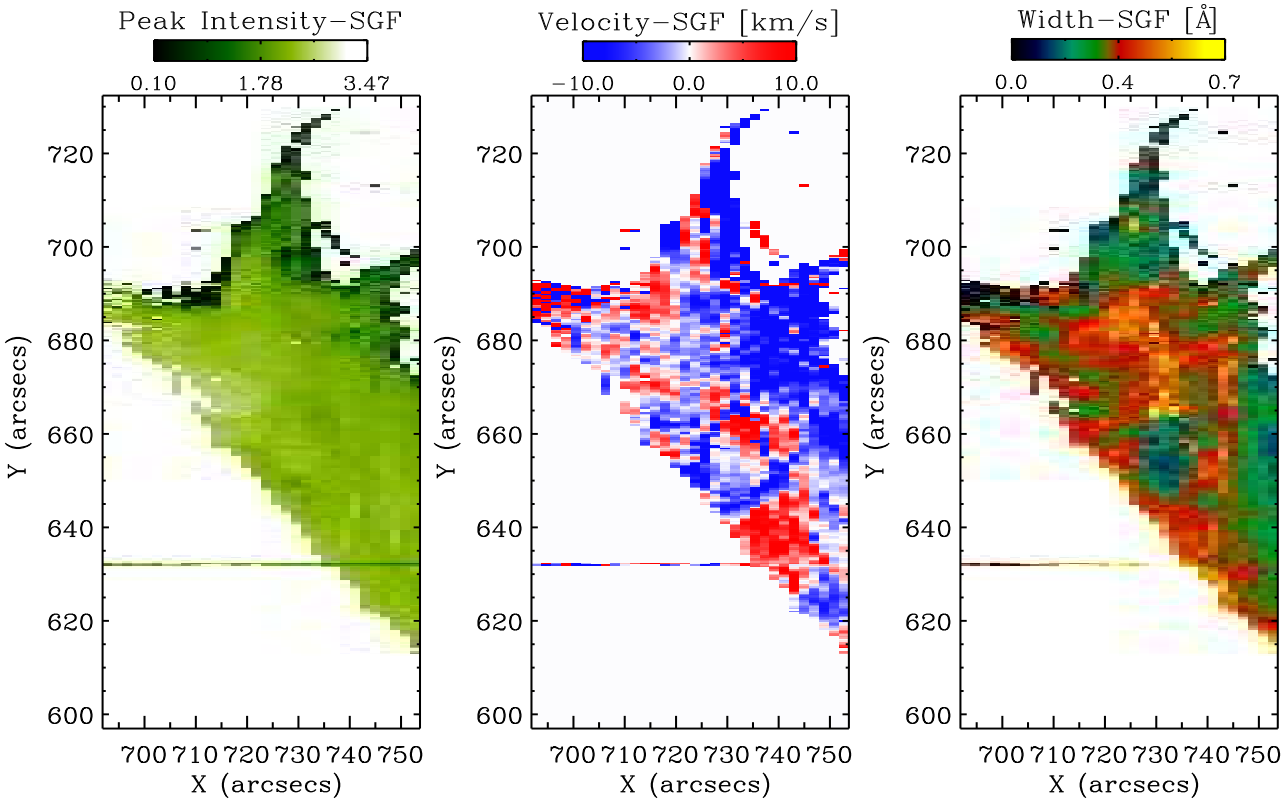


Fig. 6.— Map of peak intensity, LOS velocity and width of Mg II k obtained by fitting with the single gaussian method (SGF) of the IRIS spectra observed between 07:23:14 UT and 07:39:27 UT.

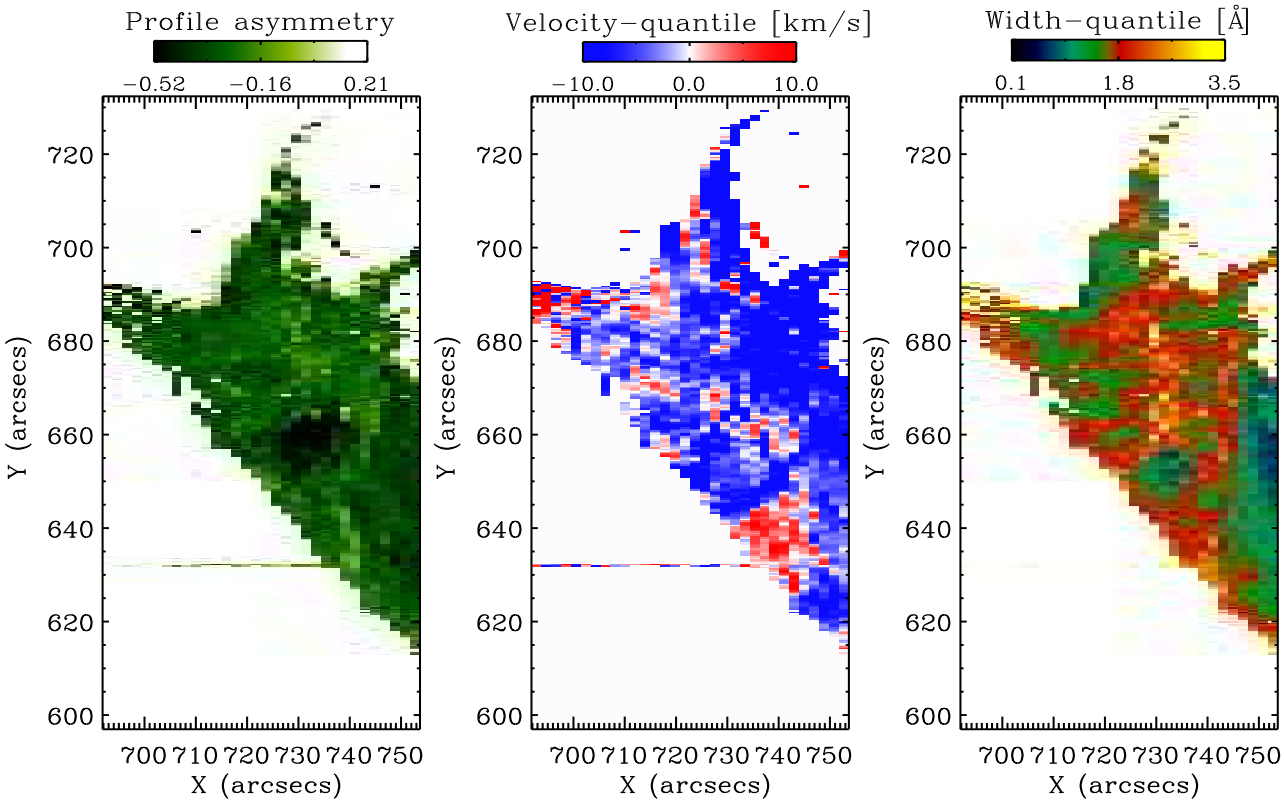


Fig. 7.— Map of profile asymmetry, LOS velocity and width of Mg II k obtained by the quantile method from the IRIS spectra observed between 07:23:14 UT and 07:39:27 UT.

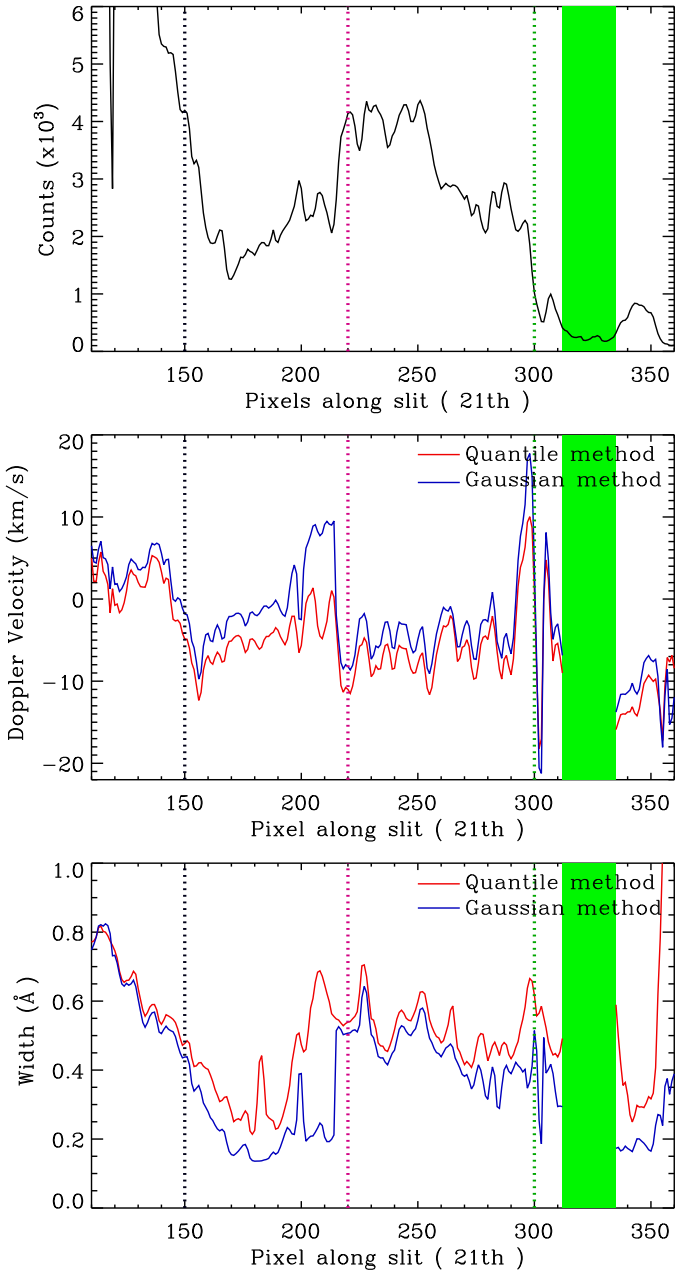


Fig. 8.— Integrated intensity along the slit 21 (seen in Figure 3 (top-left)) from -0.5 Å to 0.5 Å after fitting by a single gauss function (top panel). Dopplershift (middle panel), and line width (bottom panel) obtained with the two different methods of analysing the profiles (quantile method-red line, gaussian method- blue line). The prominence is between pixels 150 and 300. Some fine structure blobs are between pixels 340 and 350. The green band corresponds to locations where there is no emission.

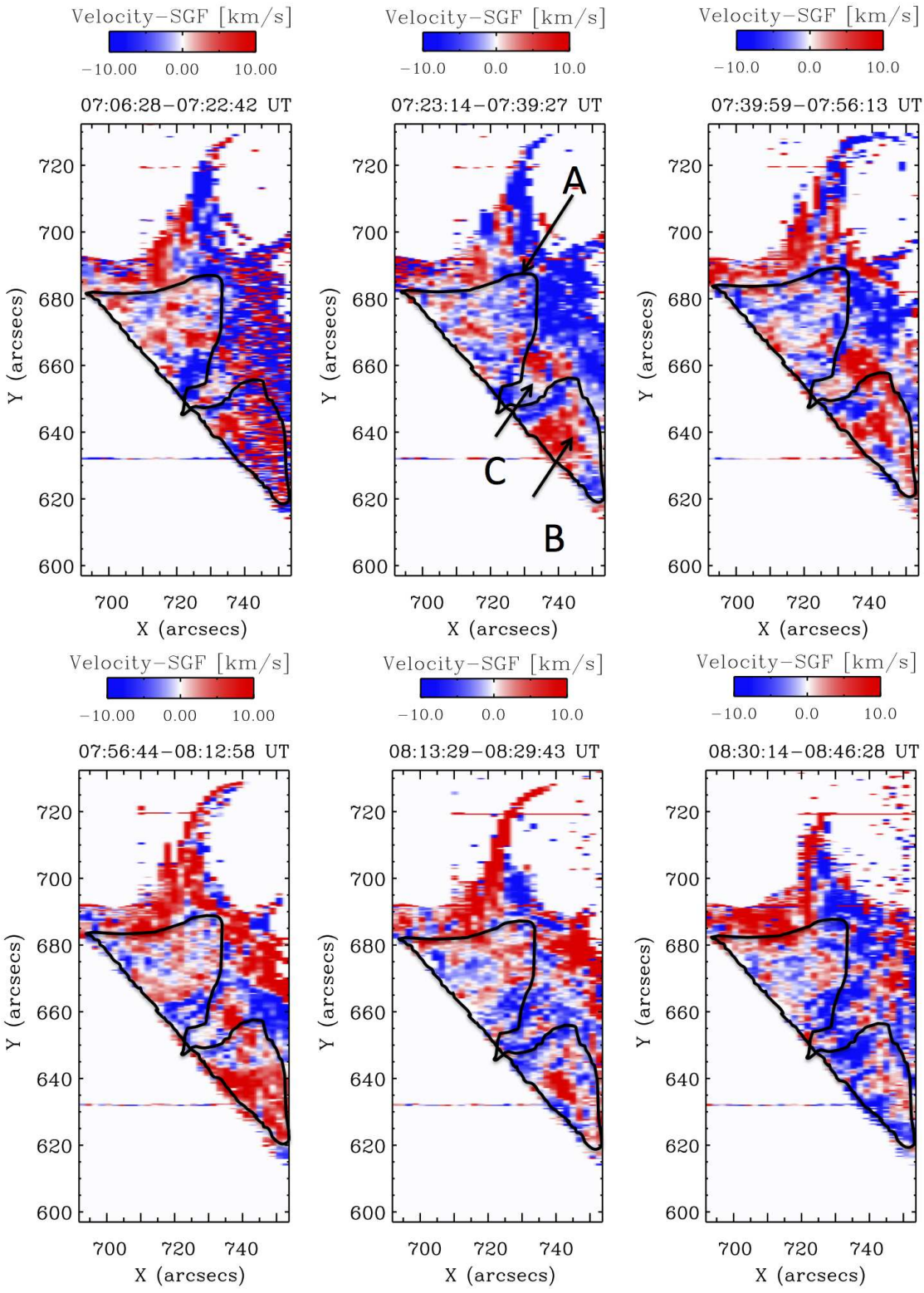


Fig. 9.— Evolution of the Dopplershift maps versus time using Mg II k line obtained from the IRIS spectra by the single gaussian fitting method (SGF). The black contour corresponds to the MSDP prominence. In the first map noisy pixels are present for x-axis between 735 arcsecs and 754 arcsecs.

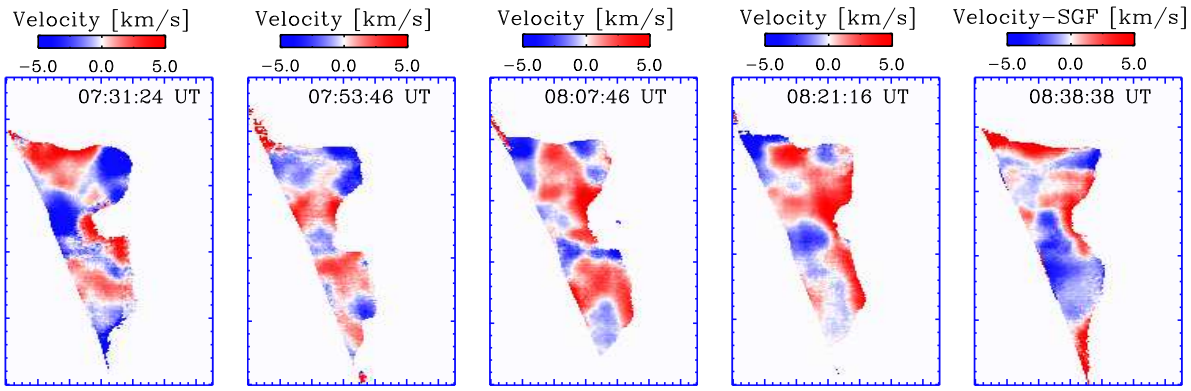


Fig. 10.— Evolution of the H$\alpha$ Dopplershift maps versus time from MSDP spectra.

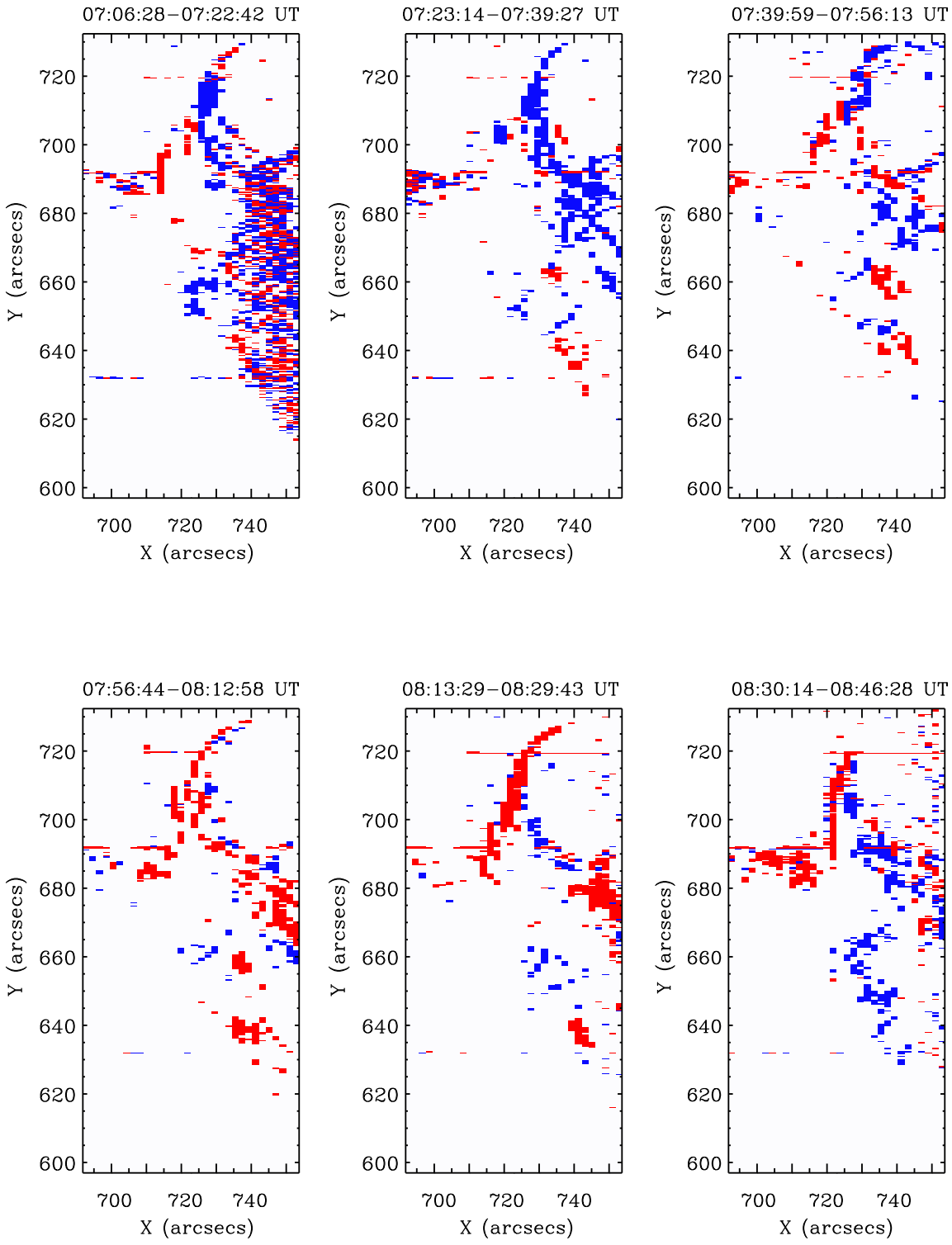


Fig. 11.— Large velocities at the edge of the prominence and the empty void or bubble with velocities higher than 9 km/s. In the first map noisy pixels are present for x-axis between 735 arcsecs and 754 arcsecs.

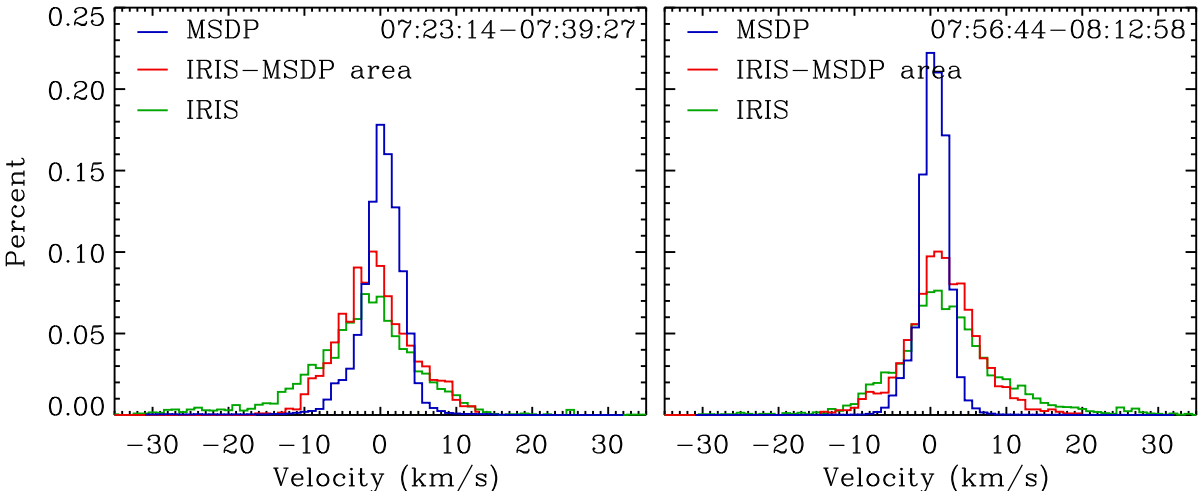


Fig. 12.— Examples of LOS velocity normalized histograms obtained for two rasters of IRIS in the Mg II k line (left panel for rasters 2 and right panel for raster 4) and for the corresponding MSDP Dopplergrams obtained in H$\alpha$ during the time interval of each IRIS raster (around 30 Doppler maps). In each panel the green line corresponds to the full prominence and the red line to the part of the prominence included in the MSDP contour (see Figure 11), the blue line corresponds to the H$\alpha$ LOS velocity histogram.

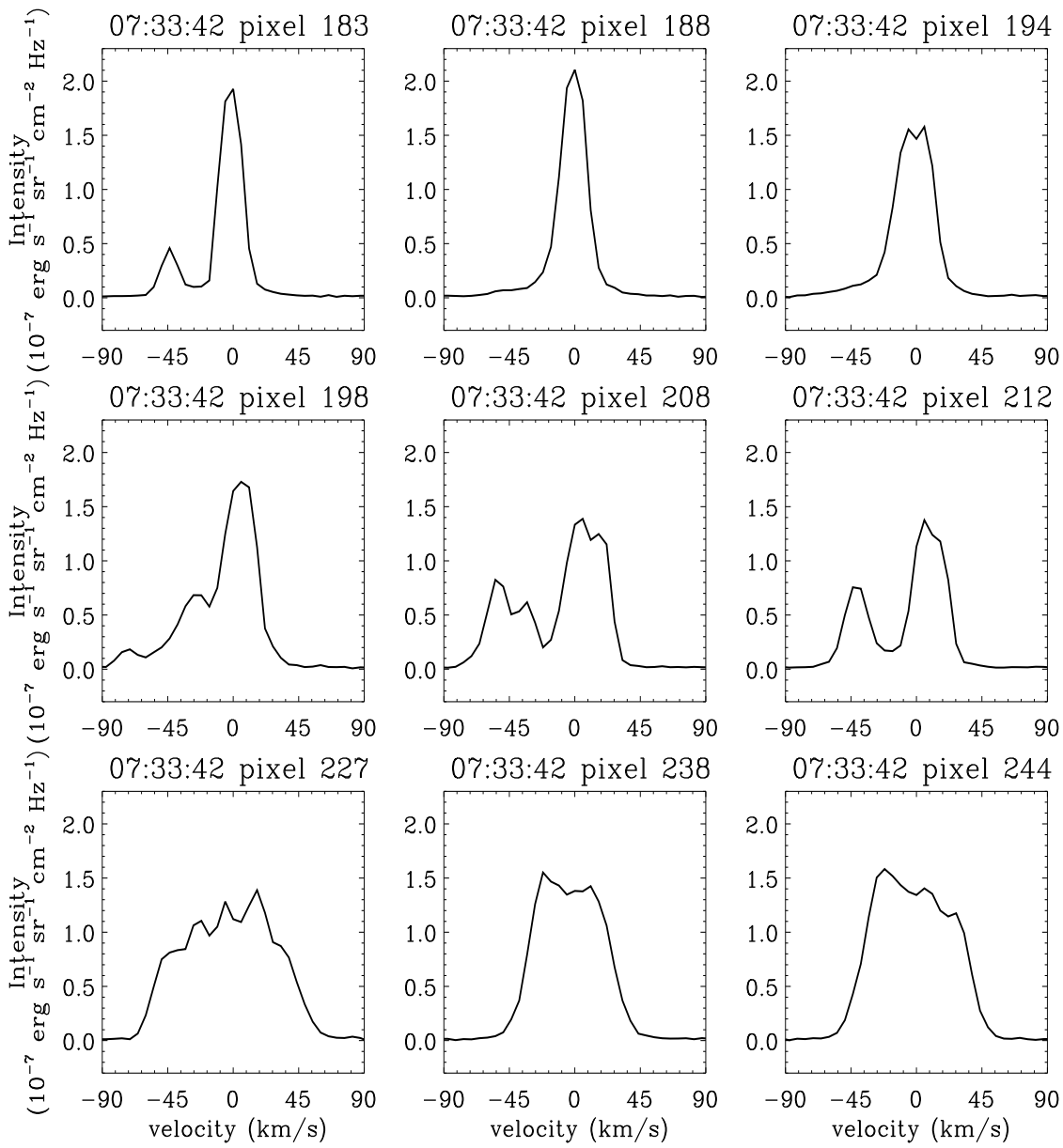


Fig. 13.— Profiles of the Mg II k line are plotted for nine selected pixels along the slit 21. The x-axis in each panel is in the units of LOS velocities. Plotted profiles show an example of different types of observed Mg II k profiles: narrow (188, 194), broad (227, 238, 244) and profiles with multiple lateral components (183, 198, 208, 212). Such a multi-component profiles indicate an existence of several fine structures along the LOS. Dopplershifts of the lateral components reach -45 km/s.

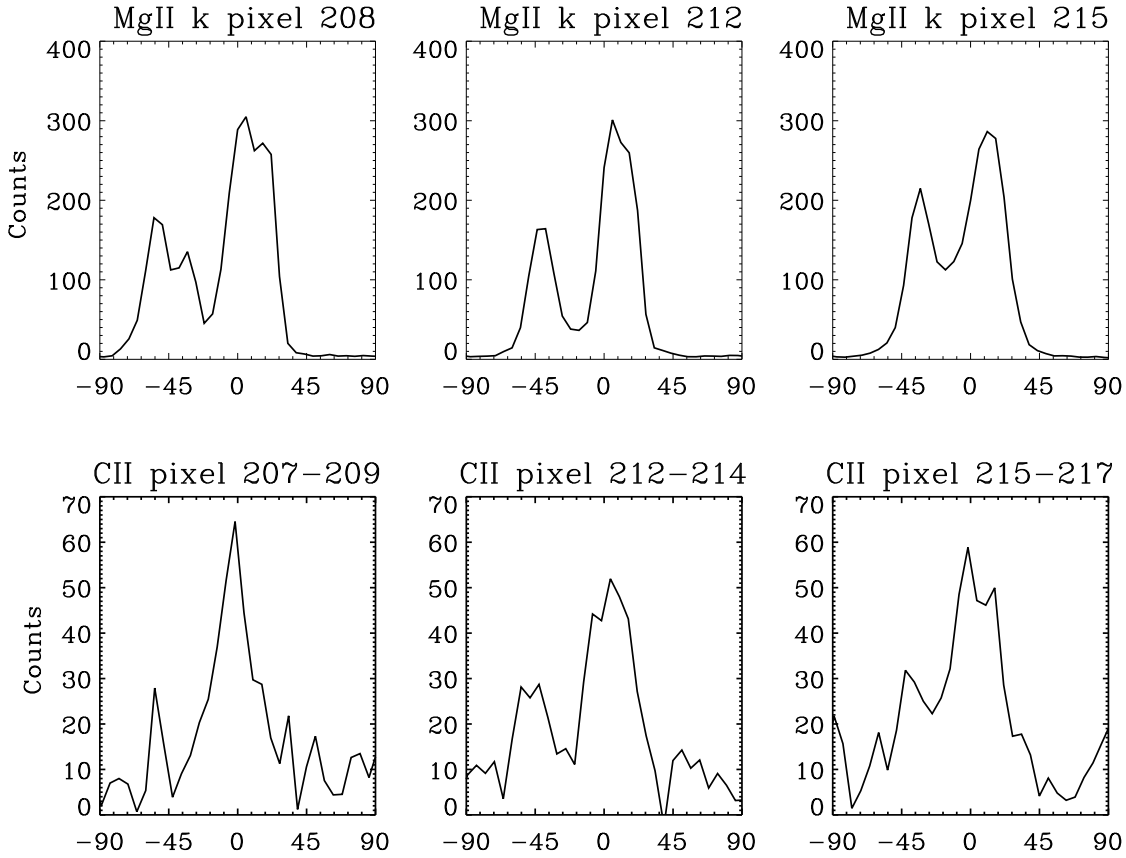


Fig. 14.— An example of distinctly multi-component profiles of the Mg II k line (top row) and the C II line (bottom). C II profiles are obtained by averaging over three adjacent pixels to increase the signal/noise ratio. The x-axis in each panel is in the units of LOS velocities.

## REFERENCES

Alissandrakis, C. E., Vial, J.-C., Koukras, A., Buchlin, E., & Chane-Yook, M. 2018, Sol. Phys., 293, 20

Aulanier, G., & Démoulin, P. 1998, A&A, 329, 1125

Berger, T. E., Shine, R. A., Slater, G. L., et al. 2008, ApJ, 676, L89

Berger, T. E., Slater, G., Hurlburt, N., et al. 2010, ApJ, 716, 1288

Chae, J., Ahn, K., Lim, E.-K., Choe, G. S., & Sakurai, T. 2008, ApJ, 689, L73

Chen, P. F., Harra, L. K., & Fang, C. 2014, ApJ, 784, 50

De Pontieu, B., Title, A. M., Lemen, J. R., et al. 2014, Sol. Phys., 289, 2733

de Toma, G., Casini, R., Burkepile, J. T., & Low, B. C. 2008, ApJ, 687, L123

Dudík, J., Aulanier, G., Schmieder, B., Bommier, V., & Roudier, T. 2008, Sol. Phys., 248, 29

Dudík, J., Aulanier, G., Schmieder, B., Zapiór, M., & Heinzel, P. 2012, ApJ, 761, 9

Goode, P. R., & Cao, W. 2012, in Proc. SPIE, Vol. 8444, Ground-based and Airborne Telescopes IV, 844403

Gunár, S., Heinzel, P., & Anzer, U. 2007, A&A, 463, 737

Gunár, S., Heinzel, P., Anzer, U., & Schmieder, B. 2008, A&A, 490, 307

Gunár, S., Mein, P., Schmieder, B., Heinzel, P., & Mein, N. 2012, A&A, 543, A93

Gunár, S., Schwartz, P., Dudik, J., Schmieder, B., & Heinzel, P. 2014, A&A

Heinzel, P., & Anzer, U. 1999, Sol. Phys., 184, 103

Heinzel, P., Schmieder, B., Mein, N., & Gunár, S. 2015, ApJ, 800, L13

Heinzel, P., Schmieder, B., Vial, J.-C., & Kotrč, P. 2001, A&A, 370, 281

Heinzel, P., Vial, J.-C., & Anzer, U. 2014, A&A, 564, A132

Heinzel, P., Schmieder, B., Fárník, F., et al. 2008, ApJ, 686, 1383

Karpen, J. T., Tanner, S. E. M., Antiochos, S. K., & DeVore, C. R. 2005, ApJ, 635, 1319

Kerr, G. S., Simões, P. J. A., Qiu, J., & Fletcher, L. 2015, A&A, 582, A50

Kosugi, T., Matsuzaki, K., Sakao, T., et al. 2007, Sol. Phys., 243, 3

Labrosse, N., Heinzel, P., Vial, J.-C., et al. 2010, Space Sci. Rev., 151, 243

Labrosse, N., & Rodger, A. S. 2016, A&A, 587, A113

Lemen, J. R., Title, A. M., Akin, D. J., et al. 2012, Sol. Phys., 275, 17

Levens, P. J., Labrosse, N., Fletcher, L., & Schmieder, B. 2015, A&A, 582, A27

Levens, P. J., Schmieder, B., Labrosse, N., & López Ariste, A. 2016a, ApJ, 818, 31

Levens, P. J., Schmieder, B., López Ariste, A., et al. 2016b, ApJ, 826, 164

Li, X., Morgan, H., Leonard, D., & Jeska, L. 2012, ApJ, 752, L22

Lin, Y., Engvold, O., Rouppe van der Voort, L., Wiik, J. E., & Berger, T. E. 2005, Sol. Phys., 226, 239

Lin, Y., Engvold, O., Rouppe van der Voort, L. H. M., & van Noort, M. 2007, Sol. Phys., 246, 65

Liu, W., De Pontieu, B., Vial, J.-C., et al. 2015, ApJ, 803, 85

Liu, Z., Xu, J., Gu, B.-Z., et al. 2014, Research in Astronomy and Astrophysics, 14, 705

Lopez-Ariste, A. L. 2014, in IAU Symposium, Vol. 300, Nature of Prominences and their Role in Space Weather, ed. B. Schmieder, J.-M. Malherbe, & S. T. Wu, 370–375

Luna, M., Karpen, J., Luís Ballester, J., et al. 2018, ArXiv e-prints

Luna, M., Karpen, J. T., & DeVore, C. R. 2012, ApJ, 746, 30

Mackay, D. H., Karpen, J. T., Ballester, J. L., Schmieder, B., & Aulanier, G. 2010, Space Sci. Rev., 151, 333

Mein, N., Schmieder, B., DeLuca, E. E., et al. 2001, ApJ, 556, 438

Rodger, A., & Labrosse, N. 2017, Solar Physics, 292, 130

Scharmer, G. B., Bjelksjo, K., Korhonen, T. K., Lindberg, B., & Petterson, B. 2003, in Society of Photo-Optical Instrumentation Engineers (SPIE) Conference Series, Vol. 4853, Innovative Telescopes and Instrumentation for Solar Astrophysics, ed. S. L. Keil & S. V. Avakyan, 341–350

Schmieder, B. 1990, in Lecture Notes in Physics, Berlin Springer Verlag, Vol. 363, IAU Colloq. 117: Dynamics of Quiescent Prominences, ed. V. Ruzdjak & E. Tandberg-Hanssen, 85–105

Schmieder, B., Chandra, R., Berlicki, A., & Mein, P. 2010, A&A, 514, A68

Schmieder, B., Kucera, T. A., Knizhnik, K., et al. 2013, ApJ, 777, 108

Schmieder, B., Malherbe, J.-M., & Wu, S. T., eds. 2014a, IAU Symposium, Vol. 300, Nature of Prominences and their role in Space Weather

Schmieder, B., Mein, N., Deng, Y., et al. 2004, Sol. Phys., 223, 119

Schmieder, B., Mein, P., Mein, N., et al. 2017a, A&A, 597, A109

Schmieder, B., Raadu, M. A., & Wiik, J. E. 1991, A&A, 252, 353

Schmieder, B., Tian, H., Kucera, T., et al. 2014b, A&A, 569, A85

Schmieder, B., Zapiór, M., López Ariste, A., et al. 2017b, A&A, 606, A30

Schmit, D. J., & Gibson, S. 2013, ApJ, 770, 35

Shen, Y., Liu, Y., Liu, Y. D., et al. 2015, ApJ, 814, L17

Su, Y., Gömöry, P., Veronig, A., et al. 2014, ApJ, 785, L2

Tandberg-Hanssen, E., ed. 1995, Astrophysics and Space Science Library, Vol. 199, The nature of solar prominences

Tandberg-Hanssen, E. 2011, Sol. Phys., 269, 237

Wang, B., Chen, Y., Fu, J., et al. 2016, ApJ, 827, L33

Wedemeyer, S., Scullion, E., Rouppe van der Voort, L., Bosnjak, A., & Antolin, P. 2013, ApJ, 774, 123

Xia, C., Keppens, R., Antolin, P., & Porth, O. 2014, ApJ, 792, L38

Yan, X.-L., Xue, Z.-K., Xiang, Y.-Y., & Yang, L.-H. 2015, Research in Astronomy and Astrophysics, 15, 1725

Yang, S., Zhang, J., Liu, Z., & Xiang, Y. 2014, ApJ, 784, L36

Yang, Z., Tian, H., Peter, H., et al. 2018, ApJ, 852, 79

Zirker, J. B., Engvold, O., & Martin, S. F. 1998, Nature, 396, 440

---

This manuscript was prepared with the AAS LaTeX macros v5.2.